Characterization of an orthotopic colorectal cancer mouse model and its feasibility for accurate quantification in positron emission tomography

Characterization of an orthotopic colorectal cancer mouse model and its feasibility for accurate quantification in positron emission tomography

Rapic Sara[1], Vangestel Christel[1,2], Verhaeghe Jeroen[1], Van den Wyngaert Tim[1,2], Hinz Rukun[3], Verhoye Marleen[3], Pauwels Patrick[4,5], Staelens Steven[1], Stroobants Sigrid[1,2]

[1]Molecular Imaging Center Antwerp (MICA), Faculty of Medicine and Health Sciences, University of Antwerp, Universiteitsplein 1, 2610 Wilrijk, Belgium

[2]Department of Nuclear Medicine, Antwerp University Hospital, Wilrijkstraat 10, 2650 Edegem, Belgium

[3]Bio-Imaging Lab (BIL), Faculty of Pharmaceutical, Biomedical and Veterinary Sciences, University of Antwerp, Universiteitsplein 1, 2610 Wilrijk, Belgium

[4]Department of Pathological Anatomy, Antwerp University Hospital, Wilrijkstraat 10, 2650 Edegem, Belgium

[5]Center for Oncological Research (CORE), Faculty of Medicine and Health Sciences, University of Antwerp, Universiteitsplein 1, 2610 Wilrijk, Belgium

Corresponding author

Prof. Dr. Sigrid Stroobants

E-mail: Sigrid.Stroobants@uza.be

Phone: +3238213696

Fax: +3238253308

Manuscript category: Original article

Running title: Imaging of Orthotopic Colorectal Cancer

Abstract

Purpose. Quantification in positron emission tomography (PET) imaging of an orthotopic mouse model of colorectal cancer (CRC) is challenging due to difficult tumor delineation. We aimed to establish a reproducible delineation approach, evaluate its feasibility for reliable PET quantification and compare its added translational value with its subcutaneous counterpart. **Procedures.** A subcutaneous Colo205-luc2 tumor fragment harvested from a donor mouse was transplanted onto the caecum of nude mice, with (n=10) or without (n=10) the addition of an X-ray detectable thread. Animals underwent [^{18}F]-fluoro-2-deoxy-D-glucose ([^{18}F]FDG) PET imaging, complemented with computed tomography (CT) and magnetic resonance imaging (MRI, 7T). Animals without a thread underwent additional contrast enhanced (Exitron) CT imaging. Tumors were delineated on the MR, μPET image or μ(CE)CT images and correlations between *in vivo* and *ex vivo* [^{18}F]FDG tumor uptake as well as between image-derived and caliper-measured tumor volume were evaluated. Finally, cancer hallmarks were assessed immunohistochemically for the characterization of both models. **Results.** Our results showed the strongest correlation between both *in vivo* and *ex vivo* uptake (r=0.84, p<0.0001) and image-derived and caliper-measured tumor volume (r=0.96, p<0.0001) when the tumor was delineated on the MR image. Orthotopic tumors displayed an abundance of stroma, higher levels of proliferation (p=0.0007), apoptosis (p=0.02) and necrosis (p<0.0001), a higher number of blood vessels (p<0.0001), yet lower tumor hypoxia (p<0.0001) as compared with subcutaneous tumors. **Conclusions.** This orthotopic mouse model proved to be a promising tool for the investigation of CRC through preclinical imaging studies provided the availability of anatomical MR images for accurate tumor delineation. Furthermore, the tumor microenvironment of the orthotopic tumor resembled more that of human CRC, increasing its likelihood to advance translational nuclear imaging studies of CRC.

Keywords: positron emission tomography, magnetic resonance imaging, contrast enhanced computed tomography, tumor delineation, orthotopic mouse model, colorectal cancer

Introduction

Metastatic colorectal cancer (CRC) is one of the leading causes of cancer-related mortality, mostly due to therapy resistance [1, 2]. Therefore, early evaluation of therapeutic efficacy is essential in order to avoid the continuation of ineffective therapy and increase the patient's survival. Fundamental research of therapy efficacy can be achieved using non-invasive, preclinical positron emission tomography (PET) imaging of CRC xenograft animals models. In these models, tumors can be engrafted ectopically or orthotopically [3, 4]. Ectopic models are typically created through implantation of tumors into the subcutaneous flank of a mouse or rat. This method is generally easy to perform and precise monitoring of tumor growth can readily be done by digital caliper measurements [5]. However, discrepancies between promising preclinical trial results and subsequent lack of clinical effect have led to the belief that traditional subcutaneous tumor models are often inadequately predictive for treatment response and are thus not optimal for translational cancer research [6-8]. Therefore, there is a renewed focus on orthotopic models, where tumors are transplanted in the same site from which the primary tumor cell lines are derived. These orthotopic tumors display highly differentiated cancer cells and an abundance of stroma, hence a more natural tumor microenvironment including angiogenic and metastatic factors [9, 10]. Consequently, orthotopic tumors are considered to more reliably mimic human cancer and thus deemed more clinically relevant for the evaluation of patient-like tumorigenesis, tumor progression and treatment response [11]. Nevertheless, orthotopic models are technically challenging and time consuming as microsurgical implantation of the tumor (cells) in the relevant mouse or rat organ is often required [12-14], complicating non-invasive follow-up of tumor location and growth. Therefore, additional imaging studies using computerized tomography (CT), magnetic resonance imaging (MRI), or optical

imaging (which requires the use of cancer cell lines expressing fluorescence or luciferase) may be needed, which are not always readily available on every site and add to the cost [15-18].

In a clinical setting, assessment of tumor response to both chemotherapy and radiotherapy relies on the detection of morphological and volumetric changes of the tumor [19]. However, changes in tumor morphology and volume are often only detectable weeks after initiation of therapy, and don't always match with tumoral molecular and metabolic response, which frequently precede these changes by weeks or even months [20, 21]. Therefore, early tumor response to therapy can be assessed with the help of molecular imaging [22]. However, particularly in CRC, the quantification of PET radiotracer uptake can be challenging due to difficult tumor delineation as a consequence of (1) constant and irregular movement of the bowels, creating image artifacts due to blurring, (2) high intestinal uptake of many tracers with consequential high background against tumor tissue and (3) the low spatial resolution of PET. In this study, we aimed to establish a reproducible orthotopic mouse model of CRC and evaluate its feasibility for accurate quantification of [^{18}F]FDG-PET, a frequently used radiotracer in the clinic for tumor imaging. Evaluation was based on the accuracy of image based tumor delineation, thereby comparing volumes of interest (VOI) delineated on PET, high-resolution MR and CT. An additional aim of this study was to characterize the tumor microenvironment of the orthotopic tumor and compare it with its subcutaneous counterpart by means of immunohistochemical staining of different cancer characteristics.

Materials and Methods

Cells and animals

A human colon cancer cell line transfected with luciferase (Colo205-luc2) was obtained from PerkinElmer. This cell line is derived from a metastatic site (ascites) from a male Caucasian patient diagnosed with Dukes type D colorectal adenocarcinoma (mutant genes: APC, BRAF, SMAD4 and TP53). The semi-adherent cells were routinely cultured in RPMI 1640 culture medium supplemented with 10 % fetal bovine serum (FBS), 1 % penicillin-streptomycin, 2 mM L-glutamine, and 1 mM sodium pyruvate (all acquired from Invitrogen). Cells were maintained at 37 °C and 5 % CO_2. Colo205-luc2 cells were used to create either subcutaneous (*n*=25) or orthotopic (*n*=20) tumors in 5-7 weeks old female athymic nude mice (Charles River). All animal experiments were approved by the local ethical committee (2012-68) and were performed in accordance with European and Belgian regulation.

Subcutaneous xenograft tumor model

Colo205-luc2 cells were harvested, washed twice in sterile phosphate buffered saline (PBS), counted and resuspended in PBS to obtain the desired concentration. Subsequently, animals were injected subcutaneously with $2x10^6$ Colo205-luc2 cells in 0.1 ml PBS in the right hind limb (*n*=25). When tumors became palpable, tumor diameters were measured 3 times a week using a digital caliper and tumor volume was approximated as: $\frac{1}{2}(length \times width^2)$. After 3 weeks, subcutaneous tumors had reached an average volume of 514±147 mm^3, with a range from 282 mm^3 to 734 mm^3. At this point, animals were euthanized through cervical dislocation and tumors were removed for transplantation (*n*=5) or immunohistochemistry (*n*=20).

Orthotopic xenograft tumor model

Orthotopic tumors were created through microsurgical transplantation of a subcutaneously grown tumor fragment harvested from donor animals (n=5, 1 tumor per four mice) onto the caecal wall of recipient mice. The removed tumor was immediately transferred to ice-cold PBS and cut into 2-3 mm^3 fragments. In half of the animals (n=10), prior to transplantation, an X-ray detectable surgical thread (Acabats i Fils, in-kind contribution) was pulled through and knotted around the tumor fragment. This barium sulphate ($BaSO_4$) covered thread has a high contrast visibility, facilitating tumor localization on CT images. Recipient mice were anesthetized with 5 % isoflurane (AbbVie) in oxygen and maintained with 1-2 % isoflurane on a heated (37 °C) pad (ThermoLux, Witte + Sutor GmbH) in supine position. The amount of delivered anesthesia was continuously monitored during surgery and adjusted manually through constant observation of the respiratory rate. First, an opioid analgesic (1 ml/kg Temgesic, Reckitt Benckiser Healthcare) was administered intramuscularly to provide pain relief. Next, the surgical site was disinfected with iso-betadine and surrounded by sterile drapes. Abdominal access was attained via a 1 cm incision through the abdominal wall musculature and peritoneal wall. The caecum was exteriorized and lavaged with sterile saline at body temperature. A tumor fragment was sutured onto the slightly damaged caecal wall (to ensure tumor cell infiltration) with two stitches using non-absorbable 4-0 surgical suture (Ethicon, Fig. 1). The caecum was returned to the abdominal cavity and skin, muscles and peritoneum were sealed with non-continuous sutures. Finally, an analgesic gel (2 % xylocaine, AstraZeneca) was applied onto the wound and the animals were allowed to recover for 2-3 days, during which period they were monitored closely for signs of inflammation or discomfort.

Image acquisition

Bioluminescence imaging

Bioluminescence imaging (BLI) of the orthotopic animals was performed on an IVIS pre-clinical optical imaging system (PerkinElmer) to assure successful tumor implantation and to monitor orthotopic tumor growth. BLI was started 7 days after surgery and continued weekly until 4 to 5 weeks after implantation, when MR/PET/CT imaging experiments commenced. Before undergoing BLI, mice were injected intraperitoneally with 150 mg/kg D-Luciferine (Promega) in PBS. After 10 min, animals were anesthetized as described before and placed onto the warmed (37 °C) stage in the scanner. BLI was conducted individually over a period of 1 s to 4 min of image acquisition.

Magnetic resonance imaging

Prior to MR/PET/CT imaging, orthotopic animals were fasted overnight (8 hours) to minimize bowel movement and maximize tumor [^{18}F]FDG uptake. Mice were anesthetized as described previously and an MR-compatible 26 G catheter (Abbocath-T Venisystems, Hospira) was inserted in the tail vein to facilitate further intravenous (*i.v.*) injections. Next, the animal was placed onto a multimodal scanner bed (Minerve) and positioned in the MR scanner. Imaging was performed on a 7 T PharmaScan MRI system (Bruker Biospin) with the Paravision 5.1 software. The physiological status of all animals was monitored throughout the imaging procedure. A pressure sensitive pad (MR-compatible Small Animal Monitoring and Gating System, SA Instruments, Inc.) was used to monitor breathing rate and a rectal thermistor with feedback controlled warm air circuitry (MR-compatible Small Animal Heating System, SA Instruments, Inc.) was used to maintain body temperature at 37.0±0.5°C. Images were acquired using

a standard Bruker 300-MHz, 38-mm transmit/receive resonator (inner diameter 7 cm). Anatomical images for tumor localization and delineation were obtained in the axial direction using a multislice (2D) T_2-weighted Rapid Acquisition with Relaxation Enhancement (RARE) sequence with an average acquisition time of 5 min. For this technique, we used 3 signal averages, an echo train length of 8, echo time of 33 ms and repetition time of 2500 ms. Field of view was (40x40x16) mm^3, spatial resolution was (0.156×0.156×0.8) mm^3 and matrix size was (256×256×20).

μPET and (contrast enhanced) CT Imaging

Immediately after the acquisition of the MR images, μPET/CT imaging was performed using two Inveon multimodality scanners (Siemens). The anesthetized mice were transported from the MR scanner to the μPET/CT scanner and injected *i.v.* using the tail vein catheter with 18.5 MBq [^{18}F]FDG. As [^{18}F]FDG clears renally and the orthotopic tumor is located in close vicinity to the bladder, diluting the radioactive urine in the bladder was necessary to avoid imaging artifacts and disguised tumor uptake. For this reason, animals were subcutaneously injected with 0.5 mg of the diuretic furosemide (Lasix, Sanofi Aventis) together with tracer administration.

During the 30-min uptake period of [^{18}F]FDG, a 10-min μCT scan was acquired with a 50 μm spot size at 80 kVp and 500 μA in 120 projections. After tracer uptake, a 20-min μPET acquisition was performed. Animals without the X-ray detectable thread (n=10) were subsequently injected *i.v.* with 0.1 ml of the nanoparticle contrast agent ExiTron nano 12000 (1200 mg iodine/kg, Miltenyi Biotec), immediately followed by an additional 10-min μCT acquisition (contrast enhanced CT or CECT). After this final μCT scan, animals were euthanized through cervical dislocation. Tumors were removed immediately and tumor volume was measured using a digital caliper. Tumor volume

was calculated as described above and ranged from 57 mm^3 to 642 mm^3, with a mean volume of 231±168 mm^3. After rinsing in PBS and weighing, tumor radioactivity was counted in an automatic gamma counter (2480 $Wizard^2$, PerkinElmer). Tumor uptake was decay and weight corrected and expressed as percentage of injected dose per gram of tissue (%ID/g). A visual overview of the creation of the orthotopic model is given in Figure 1.

Image Reconstruction and Analysis

Image reconstruction is described in *Supplemental Data*. All resulting images were analyzed using PMOD v3.3 (PMOD Technologies). μPET and μ(CE)CT images were intrinsically co-registered since they were acquired on a multimodal gantry. After manual initialization, co-registration of the MR images with the μCT images was performed automatically with the PMOD rigid matching tool using the normalized mutual information dissimilarity measure. This way, all MR images were co-registered with their corresponding μPET image through their μCT images.

For the quantification of [^{18}F]FDG tumor uptake, the orthotopic tumor was manually and independently delineated on the different images: the μPET image, the MR image and the μCT (with or without the help of the X-ray detectable thread) or μCECT image. The resulting three-dimensional VOI was applied onto the corresponding, co-registered μPET image and the averaged activity concentration (in kBq/cc) was extracted from the tumor VOI. Next, the mean percentage injected dose per cubic centimeter (%ID/cc) was calculated by dividing the activity concentration by the injected dose (in kBq) multiplied with 100 %.

Immunohistochemical Analysis

Subcutaneous (*n*=20) and orthotopic (*n*=20) tumors were fixed in 4% paraformaldehyde, embedded in paraffin and cut in 5 μm thick sections for hematoxylin and eosin (HE) staining and for immunostaining with following rabbit anti-human primary antibodies: Ki67 (proliferating cells, Cell Signaling #9027), cleaved caspase-3 (CC3, apoptotic cells, Cell Signaling #9664), carbonic anhydrase 9 (CA9, hypoxic cells, Abcam ab108351), matrix metalloproteinase-9 (MMP-9, migrating cells, Cell Signaling #13667) and von Willebrand Factor (vWF, endothelial cells, DAKO A0082). An overview of staining details is given in supplementary Table S1 and the protocols are described in *Supplemental Data*.

Stained sections were examined and analyzed under a light microscope (CX-31 RBSF, Olympus). HE stained slides were used to observe tumor differentiation and stroma. Tumor stromal areas were defined as stromal tissue surrounding groups of epithelial cancer cells in the tumor, excluding single stromal cells within groups of epithelial cancer cells. For quantification of CC3 and necrosis, pictures of the whole tumor were taken under the microscope at x200 magnification using dedicated software (NIS-Elements, Nikon). From these pictures, the ratio of CC3-positive cells over the total number of tumor nuclei, as well as the total percentage of necrosis were semi-automatically quantified using a customized segmentation program based on color thresholds and particle size (implemented in Matlab 2013a using the Image Processing Toolbox, The MathWorks Inc.). Ki67 staining was evaluated at high power field (x400 magnification) by evaluating the percentage of positively stained nuclei (from 0 to 100 %) in 10 equally sized, randomly chosen regions of interest (ROIs). The average percentage of positive cells over these 10 ROIs was then calculated. CA9 and MMP-9 were quantified by assigning to 10 random (x200) ROIs a score for both the intensity of

the staining (from 0 to 3) and the percentage (from 0 to 100 %) of positive membrane staining. To calculate the final CA9 and MMP-9 scores, the highest intensity value in each ROI was multiplied with the total percentage of positive staining in that ROI and averaged over all ROIs (H-score, adapted from [23]) . The number of blood vessels positively stained against vWF was counted in five 650x870 micron (0.6 mm^2) areas of highest vascularization at x400 magnification and averaged for each tumor section [24].

Statistical Analysis

All statistical analyses were performed using GraphPad Prism version 6.0c (GraphPad Software). Statistical significance was set at a 5 % level ($p \leq 0.05$) and all data were expressed as mean±SD. A non-directional unpaired Student's *t* test was used to determine statistical differences between two independent groups. The agreement between *in vivo* and *ex vivo* [^{18}F]FDG tumor uptake (with %ID/cc equated with %ID/g) as well as between image-derived and caliper-measured tumor volume (in mm^3) was displayed graphically by plotting the difference between the two parameters against their averages in a Bland-Altman plot. Correlations between aforementioned parameters were tested using the Pearson's correlation coefficient.

Results

Imaging of the orthotopic model

Zero mortality and a 100 % success rate (as assessed by BLI follow-up) was reached once the orthotopic model was optimized for successful tumor attachment and subsequent growth while preventing post-operative complications, including internal hemorrhaging and bowel obstruction. Figure 2 displays consecutively acquired MR, μCT, μPET and μCECT images from one representative orthotopic animal, either enhanced with the contrast agent ExiTron (n=10 from 20, Fig. 2a) or with the addition of an X-ray detectable thread (n=10 from 20, Fig. 2b). The VOI delineated around the tumor is displayed on each image. Correlations between *in vivo* and *ex vivo* [^{18}F]FDG tumor uptake as well as between image-derived and caliper-measured tumor volume for all imaging modalities are displayed in Table 1. The highest correlation between %ID/cc and %ID/g was found when the tumor was delineated on the MR image (r=0.84, p<0.0001). When the tumor was delineated directly on the μPET image without anatomical information, %ID/cc and %ID/g were significantly correlated as well (r=0.75, p=0.0001). No significant correlation could be observed for CT based delineation, neither with the help of an X-ray detectable thread (r=0.55, p=0.10) nor after administration of a contrast agent (r=0.34, p=0.34). The agreement between %ID/cc and %ID/g is displayed graphically in Figure 3 by plotting the difference between the two parameters against their averages in a Bland-Altman plot. The optimal agreement was indeed seen when the tumor was delineated on the MR image, with a difference between the upper and lower 95% limits of agreement of 5.2 %ID/g (Fig. 3a). This difference was higher for μPET- (6.8 %ID/g, Fig. 3b), μCT- (7.7 %ID/g, Fig. 3c) and μCECT- (10.6 %ID/g, Fig. 3d) based tumor delineation.

The image-based tumor volume obtained from the different VOIs was compared with the *ex vivo* caliper-based tumor volume measurement. A strong, positive correlation was seen between the MR-delineated tumor volume and the *ex vivo* caliper-measured tumor volume (r=0.96, p<0.0001). When the tumor was delineated on the μCT image, the correlation between image-delineated and caliper-measured tumor volume remained significant but diminished substantially, for both cases using an X-ray detectable thread (r=0.69, p=0.03) and CT contrast agent (r=0.64, p=0.04). The tumor volume extracted from the VOI delineated on the μPET image did not correlate with the caliper-measured tumor volume (r=0.36, p=0.12). This is also reflected in the Bland-Altman plots showing the smallest difference between the upper and lower 95% limits of agreement for MR-based tumor delineation (Fig. 4a, 176.8 mm^3), followed by μCT tumor delineation with the help of an X-ray detectable thread (Fig. 4b, 468.4 mm^3) and a contrast agent (Fig. 4c, 563 mm^3). The agreement between image-delineated and caliper-measured tumor volume was weakest when the tumor was delineated directly on the μPET image (Fig. 4b, 773.7 mm^3).

Characterization of the subcutaneous and orthotopic tumor model

The tumor microenvironment of Colo205-luc2 orthotopic (n=20) and subcutaneous (n=20) tumors was investigated by means of HE and immunostaining of important cancer hallmarks, such as proliferation, apoptosis, hypoxia, metastasis and angiogenesis. Representative images of the HE and immunostainings and their quantification are shown in Figure 5 and Table 2, respectively. HE slides of subcutaneous tumors revealed a homogenous, undifferentiated cellular rich tumor containing little or no stroma, necrosis and blood vessels. In contrast, orthotopic tumors

infiltrated the caecal crypts and were highly differentiated with an abundance of tumor stroma. A higher percentage of necrosis was seen in orthotopic tumors as compared with subcutaneous tumors ($p<0.0001$). Smaller areas of necrosis appeared focally in the tumor while eccentric, large necrotic areas were seen along the bowel and where the X-ray thread had been. Orthotopic tumors also displayed more proliferating cancer cells (Ki67, $p=0.0007$) and apoptotic bodies (CC3, $p=0.02$), exhibited a higher number of blood vessels (vWF, $p<0.0001$) and a lower level of tumor hypoxia (CA9, $p<0.0001$) as compared with subcutaneous tumors. No positive MMP-9 staining was observed in either of the tumors. The presence of the X-ray detectable thread in the orthotopic tumors did not influence the level of proliferation (Ki67, $p=0.10$), apoptosis (CC3, $p=0.67$) or hypoxia (CA9, $p=0.45$) as compared with orthotopic tumors without the thread. Orthotopic tumors growing around the thread did exhibit more necrosis ($p=0.05$) and a higher number of blood vessels (vWF, $p=0.03$).

Discussion

This study aimed at meeting the need for a reproducible approach for PET quantification in an orthotopic xenograft animal model of CRC to advance translational molecular imaging studies of CRC. The model's feasibility for accurate tracer uptake quantification based on tumor delineation on different imaging modalities (μPET, MR image, μCT with or without CT contrast agent or X-ray detectable thread) was evaluated. Correlations between *in vivo* and *ex vivo* (gold standard) [^{18}F]FDG tumor uptake as well as between image-derived and caliper-measured tumor volume were assessed. For both parameters, tumor delineation on the MR image led to the most accurate quantification of the [^{18}F]FDG PET signal.

Our results showed the strongest correlation between both the *in vivo* and *ex vivo* uptake and the image-derived and caliper-measured tumor volume when the tumor was delineated on the MR image. Tumor volume extracted from the μCT images did not correlate with caliper-measured tumor volume, yet with the help of the X-ray thread or contrast agent, the two parameters correlated significantly. Although assisting in tumor localization, the addition of an X-ray detectable thread or contrast agent did not lead to a correlation between *in vivo* and *ex vivo* uptake. These findings are in agreement with the general notion that MR imaging provides excellent soft tissue contrast while μCT suffers from poor soft tissue contrast. Although other studies observed improved soft tissue contrast with ExiTron nano [25] and enhanced tumor contrast to the surrounding tissue [26], it should be noted that contrast enhancement of the tumor greatly depends on the level of tumor vascularization and perfusion, which was generally low in our tumor model. Furthermore, ExiTron nano revealed a level of toxicity, as a mortality of 20% was observed shortly after *i.v.* injection, according to manufacturer's instructions, an undesirable side-effect experienced by other researchers [27, 28]. When the tumor

was delineated directly on the μPET image, no correlation was found between image-based and caliper-measured tumor volume. This mismatch is not surprising since [^{18}F]FDG-PET estimates the metabolic volume rather than the true volume. In our case, true volume was underestimated by PET-based delineation, most likely due to necrotic areas at the tumor border without tracer uptake, which would not have been included in tumor delineation. The μPET-based tumor delineation led to a positive, significant correlation between *in vivo* and *ex vivo* uptake, confirming the tumor was indeed correctly localized in the μPET image, a crucial prerequisite to reach this level of agreement. In our study, we observed a high baseline [^{18}F]FDG uptake in the Colo205-luc2 tumor against the low intestinal background uptake of [^{18}F]FDG, facilitating tumor localization and delineation without the inclusion of surrounding bowel tissue. Nevertheless, many PET tracers show a generally elevated intestinal uptake, which could considerably complicate discrimination between tumor and bowel tissue on the μPET image [29]. Also, the addition of therapy can influence tracer uptake, potentially reducing the PET signal drastically. Taken together, our results bring forward the anatomical MR image as superior for accurate tumor delineation.

The orthotopic tumor clearly reflected the morphological characteristics of an advanced human CRC, with a high proliferation rate and areas of necrosis, as well as increased neo-angiogenesis, increasing the likelihood of it being a more predictive and translational model of CRC. Similarly, Céspedes and colleagues observed in their CRC orthotopic mouse model many necrotic areas and a high mitotic count [30]. Nevertheless, a high level of necrosis could affect the consistency of the model. The necrotic areas bordering the caecal wall, the place of transplantation and infiltration, are most likely the outcome of the continuous demand of oxygen and nutrients of the cancer cells to maintain a proliferative state, characteristic for a fast-growing tumor. Large

areas of necrosis were also noticeable surrounding the X-ray detectable thread. Nevertheless, the presence of a foreign material did not influence tumor growth, nor did it affect [^{18}F]FDG uptake. In fact, from historic data obtained in our lab with the Colo205 subcutaneous model [31], we have calculated baseline [^{18}F]FDG uptake to be three times more elevated in the orthotopic tumors (p<0.0001, *data not shown*). Based on the (immuno)histological data obtained from these tumors, we hypothesized this to be the result of the increased number of proliferating cells as well as inflammatory cells, which are likely pro-inflammatory cancer-associated fibroblasts [32] or originate from the host's immune response to the introduction of a foreign body. As inflammation is a process that requires energy, and [^{18}F]FDG is a glucose analogue, it is known to be taken up by inflammatory cells [33]. It is worth noting that, at the time of IHC evaluation, the tumor volume of the orthotopic tumors was on average half of that of the subcutaneous tumors. This too could contribute to the higher level of proliferation, as the growth fraction of the smaller, orthotopic tumors is likely to be higher.

Spontaneously metastasizing animal cancer models are considered clinically relevant. While subcutaneous tumors almost always fail to metastasize, orthotopic tumors often mimic the metastatic profile of human cancer [30]. Our orthotopic tumors, however, did not express MMP-9, a matrix metalloproteinase closely linked to cancer metastasis. With our time schedule of 4 to 5 weeks after transplantation, it is possible that the primary tumor did not have enough time to develop a metastatic phenotype. Other studies of orthotopic CRC models only detected metastasized cancer cells to other organs after 7-8 [34] to 16 weeks after inoculation [9]. Taken together, the tumor microenvironment of our CRC orthotopic model differed from its subcutaneous counterpart, resembling more that of human CRC. Longitudinal studies of the model can determine its metastatic potential.

Conclusions

The reproducible orthotopic mouse model proves to be a promising tool for the investigation of CRC through preclinical imaging studies. For accurate tumor delineation, anatomical MRI is advisable as CT imaging, either aided by an X-ray detectable thread or enhanced with contrast, did not offer sufficient soft tissue contrast in our hands. Immunohistochemical evaluation demonstrated the added physiological value of the orthotopic model, likely due to the effects of a more natural tumor microenvironment. Future studies with this model will allow *in situ* evaluation of CRC tumorigenesis, tumor progression and therapy response by means of non-invasive molecular imaging.

Acknowledgements

The authors thank Philippe Joye and Caroline Berghmans of the Molecular Imaging Center Antwerp as well as Johan Van Audekerke of the Bio-Imaging Lab for their valuable technical assistance. This work was funded by the University of Antwerp through a Bijzonder Onderzoeksfond for S.R. (BOF27327) and the iMinds ICON project FIAT (Functional Image Analysis of Tumors) for J.V., M.V. and R.H. Si.S and C.V. are supported by the Innovative Medicines Initiative Joint Undertaking (www.imi.europa.eu) under grant agreement number 115151, resources of which are composed of financial contribution from the European Union's Seventh Framework Program (FP7/2007-2013) and EFPIA companies' in-kind contribution.

Conflict of interest

The authors declare that they have no conflict of interest.

References

1. Torre LA, Bray F, Siegel RL, et al (2015) Global Cancer Statistics, 2012. CA-Cancer J Clin 65:87–108.

2. Wilson PM, Labonte MJ, Lenz H-J (2010) Molecular markers in the treatment of metastatic colorectal cancer. Cancer J 16:262–272.

3. Jung J (2014) Human tumor xenograft models for preclinical assessment of anticancer drug development. Toxicol Res 30:1–5.

4. Teicher BA (2006) Tumor models for efficacy determination. Mol Cancer Ther 5:2435–2443.

5. Morton CL, Houghton PJ (2007) Establishment of human tumor xenografts in immunodeficient mice. Nature Protocols 2:247–250.

6. Talmadge JE, Singh RK, Fidler IJ, Raz A (2007) Murine models to evaluate novel and conventional therapeutic strategies for cancer. Am J Pathol 170:793–804.

7. Johnson JI, Decker S, Zaharevitz D, et al (2001) Relationships between drug activity in NCI preclinical in vitro and in vivo models and early clinical trials. Br J Cancer 84:1424–1431.

8. Rubio-Viqueira B, Hidalgo M (2009) Direct In Vivo Xenograft Tumor Model for Predicting Chemotherapeutic Drug Response in Cancer Patients. Clin Pharmacol Ther 85:217–221.

9. Hackl C, Man S, Francia G, et al (2012) Metronomic oral topotecan prolongs survival and reduces liver metastasis in improved preclinical orthotopic and adjuvant therapy colon cancer models. Gut 62:259–71.

10. Bibby MC (2004) Orthotopic models of cancer for preclinical drug evaluation. Eur J Cancer 40:852–857.

11. Hoffman RM (1999) Orthotopic metastatic mouse models for anticancer drug discovery and evaluation: A bridge to the clinic. Invest New Drugs 17:343–359.

12. Tseng W, Leong X, Engleman E (2007) Orthotopic Mouse Model of Colorectal Cancer. JoVE 10:484.

13. Tseng WW, Winer D, Kenkel JA, et al (2010) Development of an Orthotopic Model of Invasive Pancreatic Cancer in an Immunocompetent Murine Host. Clin Cancer Res 16:3684–3695.

14. Pavese J, Ogden IM, Bergan RC (2013) An Orthotopic Murine Model of Human Prostate Cancer Metastasis. JoVE 79:e50873.

15. Haldorsen IS, Popa M, Fonnes T, et al (2015) Multimodal Imaging of Orthotopic Mouse Model of Endometrial Carcinoma. PLoS ONE 10:e0135220.

16. Cao HST, Kaushal S, Snyder CS, et al (2010) Real-time Imaging of Tumor Progression in a Fluorescent Orthotopic Mouse Model of Thyroid Cancer. Anticancer Res 30:4415–4422.

17. Yahyanejad S, Granton PV, Lieuwes NG, et al (2015) Complementary Use of Bioluminescence Imaging and Contrast-Enhanced Micro-Computed Tomography in an Orthotopic Brain Tumor Model. Mol Imaging.

18. Partecke IL, Kaeding A, Sendler M, et al (2011) In vivo imaging of pancreatic tumours and liver metastases using 7 Tesla MRI in a murine orthotopic pancreatic cancer model and a liver metastases model. BMC Cancer.

19. Eisenhauer EA, Therasse P, Bogaerts J, et al (2009) New response evaluation criteria in solid tumours: Revised RECIST guideline (version 1.1). Eur J Cancer 45:228–247.

20. Weber DC, Zilli T, Buchegger F, et al (2008) [(18)F]Fluoroethyltyrosine-positron emission tomography-guided radiotherapy for high-grade glioma. Radiat Oncol 3:44.

21. Van den Abbeele AD (2008) The lessons of GIST - PET and PET/CT: A new paradigm for imaging. Oncologist 13:8–13.

22. Kircher MF, Hricak H, Larson SM (2012) Molecular imaging for personalized cancer care. Mol Oncol 6:182–195.

23. Mees G, Vangestel C, Dierckx R, et al (2010) Carbonic Anhydrase IX Expression Correlates with FDG Uptake by Primary Non-Small Cell Lung Cancer. Cancer Biother Radiopharm 25:149–154.

24. Maeda K, Chung YS, Takatsuka S, et al (1995) Tumour angiogenesis and tumour cell proliferation as prognostic indicators in gastric carcinoma. Br J Cancer 72:319–323.

25. Mannheim JG, Schlichthaerle T, Kuebler L, et al (2016) Comparison of small animal CT contrast agents. Contrast Media Mol Imaging 11:272–284.

26. Boll H, Nittka S, Doyon F, et al (2011) Micro-CT Based Experimental Liver Imaging Using a Nanoparticulate Contrast Agent: A Longitudinal Study in Mice. PLoS ONE 6:e25692.

27. Nebuloni L, Kuhn GA, Mueller R (2013) A Comparative Analysis of Water-

Soluble and Blood-Pool Contrast Agents for in vivo Vascular Imaging with Micro-CT. Acad Radiol 20:1247–1255.

28. Wathen CA, Foje N, van Avermaete T, et al (2013) In vivo X-Ray Computed Tomographic Imaging of Soft Tissue with Native, Intravenous, or Oral Contrast. Sensors 13:6957–6980.

29. Wahl RL (2004) Why nearly all PET of abdominal and pelvic cancers will be performed as PET/CT. J Nucl Med 45:82S–95S.

30. Céspedes MV, Espina C, García-Cabezas MA, et al (2007) Orthotopic microinjection of human colon cancer cells in nude mice induces tumor foci in all clinically relevant metastatic sites. Am J Pathol 170:1077–1085.

31. De Bruycker S, Vangestel C, Van den Wyngaert T, et al (2016) Baseline [18F]FMISO μPET as a Predictive Biomarker for Response to HIF-1α Inhibition Combined with 5-FU Chemotherapy in a Human Colorectal Cancer Xenograft Model. Mol Imaging Biol 18:606–616.

32. Mukaida N, Sasaki S (2016) Fibroblasts, an inconspicuous but essential player in colon cancer development and progression. World J Gastroenterol 22:5301–5316.

33. Love C, Tomas MB, Tronco GG, Palestro CJ (2005) FDG PET of infection and inflammation. Radiographics 25:1357–1368.

34. Rajput A, Agarwal E, Leiphrakpam P, et al (2013) Establishment and Validation of an Orthotopic Metastatic Mouse Model of Colorectal Cancer. ISRN Hepatol 2013:206875.

Tables

Table 1. Correlations for different imaging modalities

	MRI	PET	CT	CT (X-ray)	CECT
[^{18}F]FDG uptake	$r = 0.84$ *$p < 0.0001$*	$r = 0.75$ *$p = 0.001$*	$r = 0.26$ $p = 0.47$	$r = 0.55$ $p = 0.10$	$r = 0.34$ $p = 0.34$
Tumor volume	$r = 0.96$ *$p < 0.0001$*	$r = 0.36$ $p = 0.12$	$r = 0.57$ $p = 0.08$	$r = 0.69$ *$p = 0.03$*	$r = 0.64$ *$p = 0.04$*

r = Pearson's r, p = p-value
Statistically significant p-values are marked in *italics*.

Table 2. IHC units and scores

Cancer hallmark	Unit	Subcutaneous tumor	Orthotopic tumor	*p*-value
Proliferation (Ki67)	Percentage positively stained cells	73.6±6.0	80.2±6.0	0.0007
Hypoxia (CA9)	H-score	117.5±25	69.6±17	<0.0001
Angiogenesis (vWF)	Microvessel density/0.6 mm^2	4.7±1.0	12.5±5.0	<0.0001
Apoptosis (CC3)	Ratio of CC3-positive cells over total tumor nuclei	0.83±0.7	1.30±0.5	0.02
Necrosis	Percentage necrotic area	0.53±0.43	7.0±3.6	<0.0001

All values are expressed as mean ± SD.

Figures

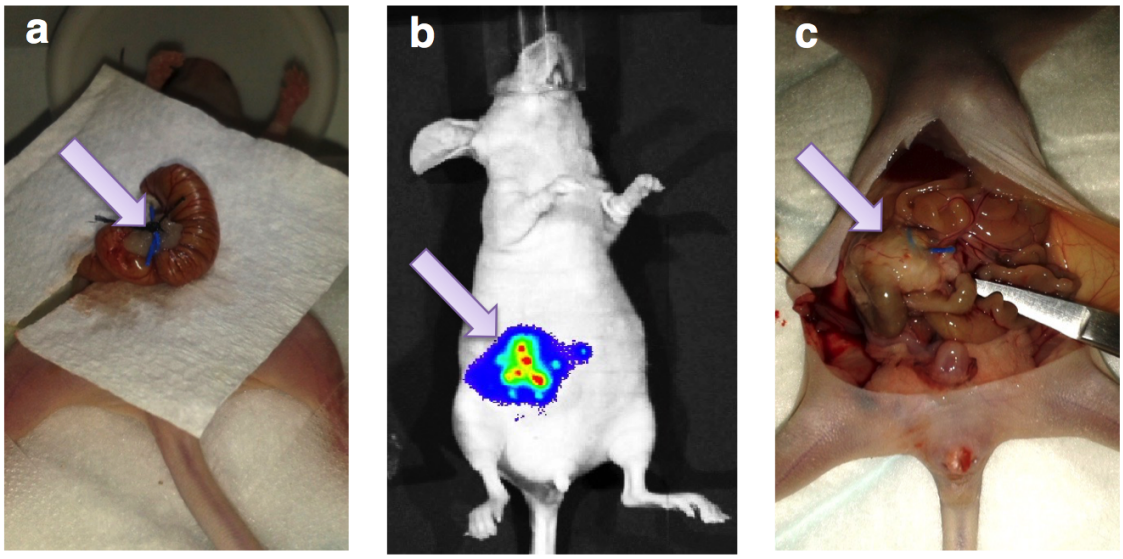

Figure 1. Creation of the orthotopic model. (**a**) A subcutaneously grown tumor fragment (2-3 mm^3) was microsurgically transplanted onto a recipient's mouse colon, with or without the addition of an X-ray detectable thread (*blue*). (**b**) Transplantation success and tumor growth were followed up weekly using BLI. (**c**) Typically 4-5 weeks after transplantation, μPET/(CE)CT/MR imaging was performed, after which the mouse was euthanized for further *ex vivo* validation using gamma counting and IHC. *Arrows* point out tumors.

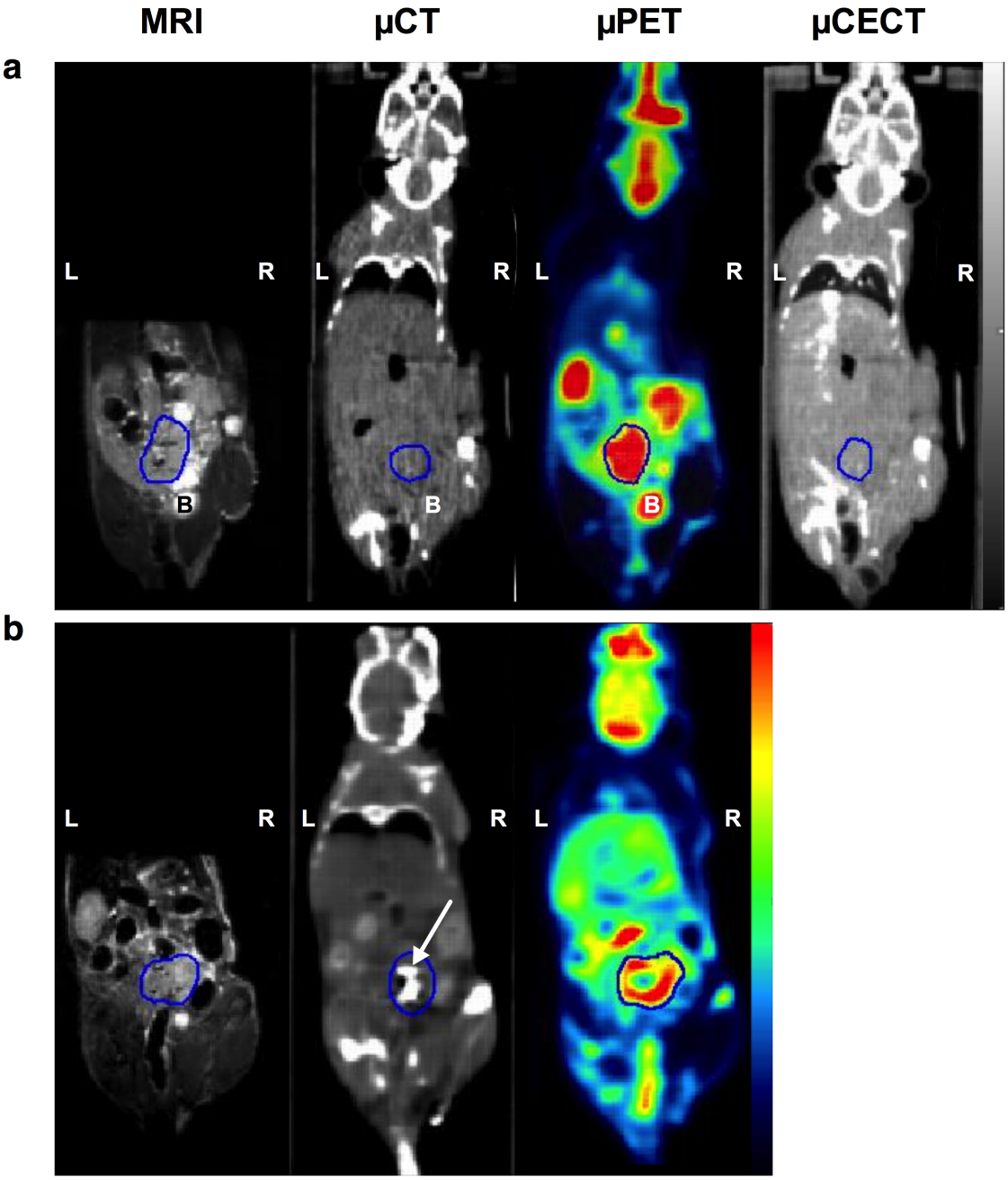

Figure 2. Imaging of the orthotopic model. Tumor delineation (*blue VOI*) on *-from left to right-* MR, µCT, µPET and µCECT images acquired consecutively from a representative animal without **(a)** and with **(b)** an X-ray detectable thread (*white arrow*). *B* = bladder, *R* = right, *L* = left

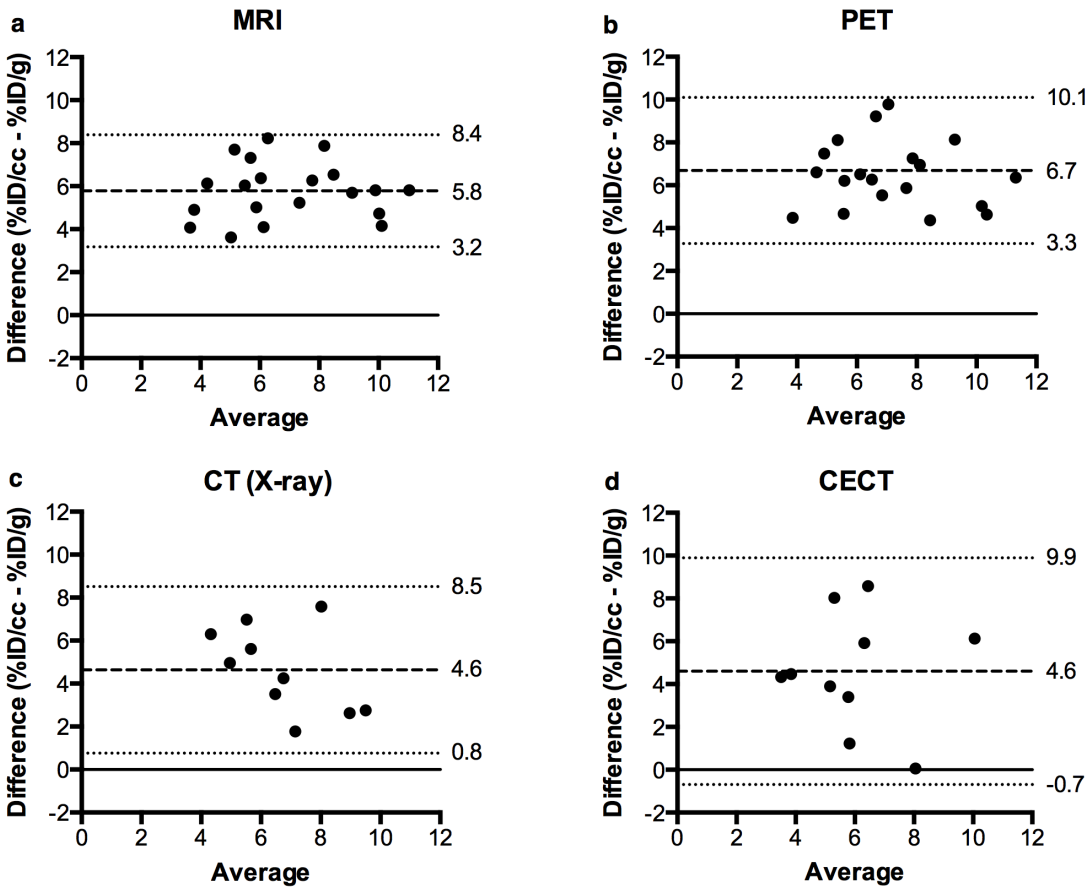

Figure 3. Bland-Altman plots show the difference between %ID/g and %ID/cc calculated from activity in the tumor VOI as delineated on the MR image **(a)**, μPET image **(b)** or μCT image including the X-ray detectable thread **(c)** or a contrast agent **(d)**. The *dashed* and *dotted horizontal lines* indicate the mean difference and the 9 5% limits of agreement (mean difference±1.96 x SD of the differences), respectively. The *solid horizontal line* is drawn at *y*=0.

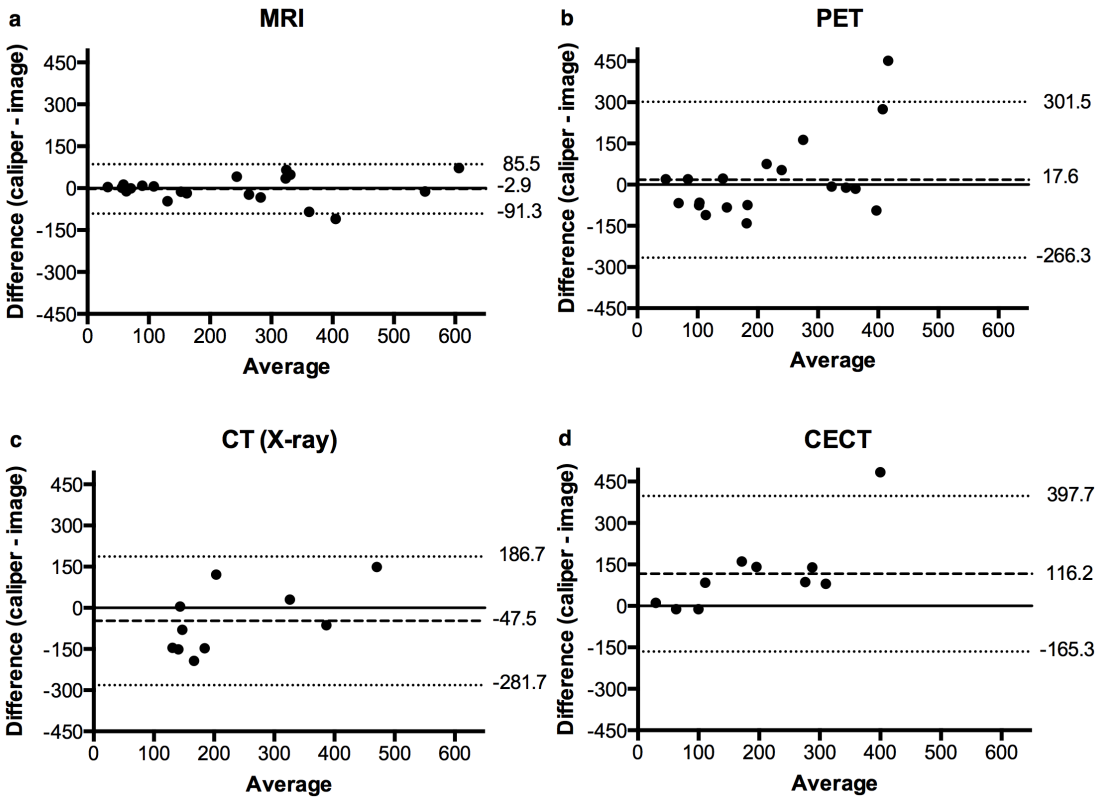

Figure 4. Bland-Altman plots show the difference between the tumor volume calculated from *ex vivo* digital caliper measurements of the tumor diameters and the tumor volume determined from the tumor VOI as delineated on the MR image **(a),** µPET **(b)** or µCT image including the X-ray detectable thread **(c)** or a contrast agent **(d)**. The *dashed* and *dotted horizontal lines* indicate the mean difference and the 95 % limits of agreement (mean difference±1.96 x SD of the differences), respectively. The *solid horizontal line* is drawn at y=0.

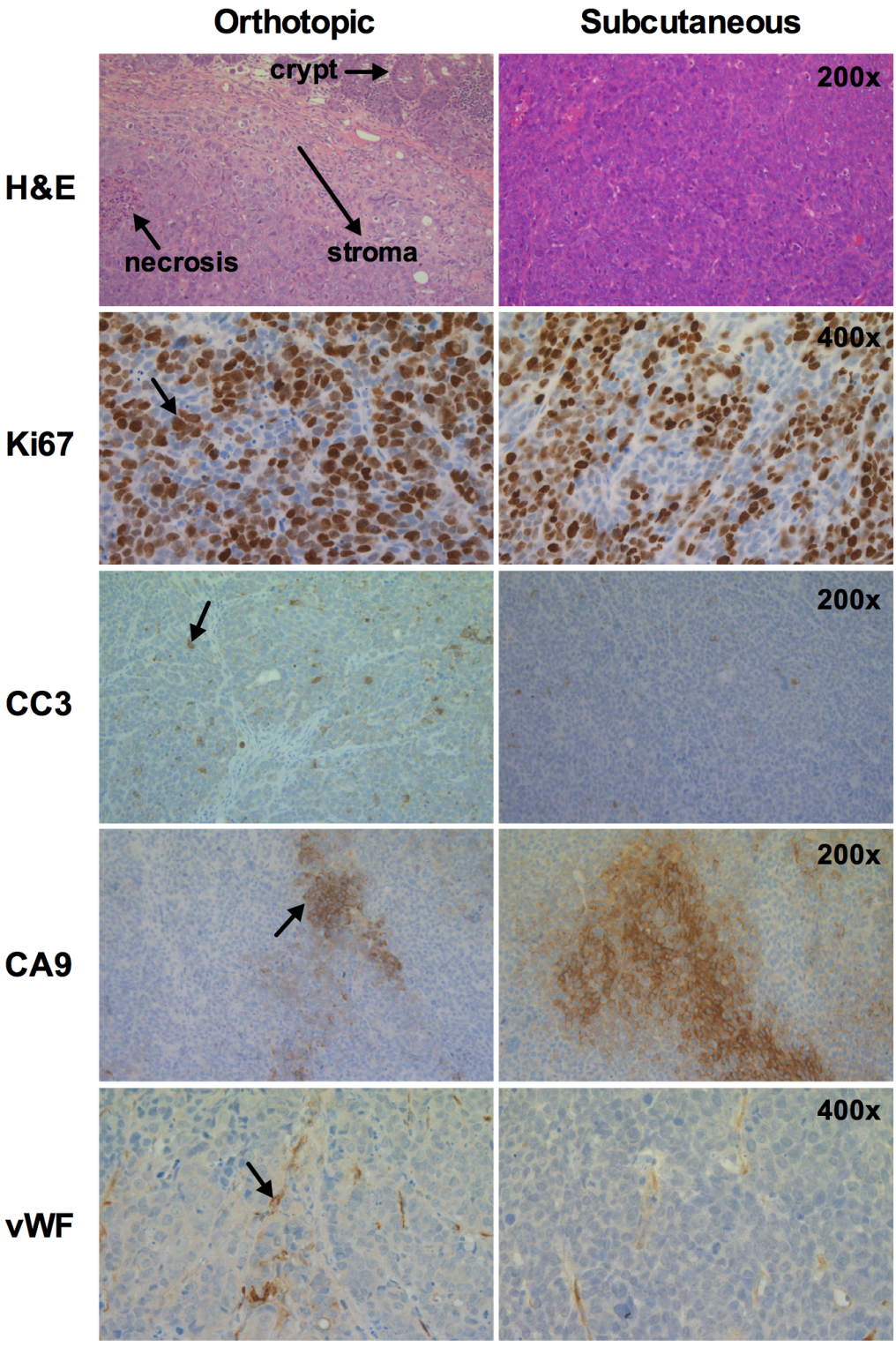

Figure 5. Characterization of the orthotopic model. Photographs of representative slides from orthotopic (left) and subcutaneous (right) tumors stained with H&E and against Ki67, CC3, CA9, MMP-9 and vWF (*from top to bottom*). Positively stained areas are colored brown and indicated with a *black arrow*.